

PAPER

Giant optical anisotropy of WS₂ flakes in the visible region characterized by Au substrate assisted near-field optical microscopy

To cite this article: Nan Deng *et al* 2022 *Nanotechnology* **33** 345201

View the [article online](#) for updates and enhancements.

You may also like

- [First-principles study of the impact of chemical doping and functional groups on the absorption spectra of graphene](#)
Iyyappa Rajan Panneerselvam, Pranay Chakraborty, Qiong Nian *et al.*
- [Wide-viewing-angle flexible liquid crystal displays with optical compensation of polycarbonate substrates](#)
Takahiro Ishinabe, Akihito Sato and Hideo Fujikake
- [Characterization of optical properties and thermo-optic effect for non-polar AlGaIn thin films using spectroscopic ellipsometry](#)
Shuai Chen, Xiong Zhang, Aijie Fan *et al.*





IOP | ebooks™

Bringing together innovative digital publishing with leading authors from the global scientific community.

Start exploring the collection—download the first chapter of every title for free.

Giant optical anisotropy of WS₂ flakes in the visible region characterized by Au substrate assisted near-field optical microscopy

Nan Deng¹, Hua Long^{1,*} , Kun Wang¹, Xiaobo Han², Bing Wang¹, Kai Wang^{1,*}  and Peixiang Lu^{1,2,3,*}

¹ Wuhan National Laboratory for Optoelectronics and School of Physics, Huazhong University of Science and Technology, Wuhan 430074, People's Republic of China

² Hubei Key Laboratory of Optical Information and Pattern Recognition, Wuhan Institute of Technology, Wuhan 430205, People's Republic of China

³ Optics Valley Laboratory, Wuhan 430074, People's Republic of China

E-mail: longhua@hust.edu.cn, kale_wong@hust.edu.cn and lupeixiang@hust.edu.cn

Received 10 March 2022, revised 22 April 2022

Accepted for publication 4 May 2022

Published 31 May 2022



Abstract

Transition metal dichalcogenides (TMD) have attracted considerable attention in the field of photonic integrated circuits due to their giant optical anisotropy. However, on account of their inherent loss in the visible region and the difficulty of measuring high refractive index materials, near-field characterizations of the optical anisotropy of TMD in the visible region have inherent experimental difficulties. In this work, we present a systematical characterization of the optical anisotropy in tungsten disulfide (WS₂) flakes by using scattering-type scanning near-field optical microscopy (*s*-SNOM) excited at 671 nm. Transverse-electric and transverse-magnetic (TM) waveguide modes can be excited in WS₂ flakes with suitable thickness, respectively. With the assistance of the Au substrate, the contrast of the near-field fringes is enhanced in comparison with the SiO₂ substrate. By combining waveguide mode near-field imaging and theoretical calculations, the in-plane and out-of-plane refractive indexes of WS₂ are determined to be 4.96 and 3.01, respectively, indicating a high birefringence value up to 1.95. This work offers experimental evidence for the potential application of WS₂ in optoelectronic integrated circuits in the visible region.

Supplementary material for this article is available [online](#)

Keywords: optical anisotropy, WS₂ flakes, near-field characterizations, visible-region waveguides

(Some figures may appear in colour only in the online journal)

1. Introduction

Giant optical anisotropy materials have emerged as an essential role in light manipulation. Birefringence crystals exhibiting optical anisotropy are the fundamental components of phase retardation elements, such as waveplates and phase-matching elements [1–3]. The phase difference between the different modes in phase retardation elements is proportional

to the transmission distance of the modes, as well as the thickness and the birefringence of the materials [4]. Consequently, materials with higher birefringence values offer a good candidate for light manipulations, which is conducive to making compact and efficient optical devices [5, 6]. In general, birefringence materials are inorganic crystals [7], liquid crystals [8, 9], and some artificial semiconductor nanostructures [10], but their maximum birefringence value is less than 0.8. By comparison, transition metal dichalcogenides (TMD) show a much larger optical anisotropy due to the

* Authors to whom any correspondence should be addressed.

symmetry breaking, which is ascribed to the fundamental differences between intralayer strong covalent bonding and weak interlayer van der Waals interaction [11]. Therefore, TMD offer a very promising candidate for the smaller and more energy-efficient structures in integrated nanophotonics [12].

High-quality 2D layered materials are usually obtained by the mechanical exfoliation processes from bulk TMD crystals, producing flakes with a size of micrometers and the thickness of nanometers [13–15]. In general, far-field spectroscopic techniques, including reflectance, transmittance, and ellipsometry measurements, are used to characterize the optical properties of TMD flakes. However, the atomic thickness of TMD flakes limits the length of light–matter interaction, indicating a very weak effective signal for the mentioned techniques. Therefore, it is a challenging task to measure the anisotropic optical response of the exfoliated TMD crystals [16]. Recently, scattering-type scanning near-field optical microscopy (*s*-SNOM) has been used to quantitatively characterize the optical anisotropy of TMD flakes [17, 18]. By mapping the waveguide modes in real space, the birefringence index of TMD flakes can be determined. Previously, this near-field method is mainly applied in measuring van der Waals flakes in the near- and mid-infrared region, many novel discoveries have been reported, such as volume-confined hyperbolic polaritons [19–22], surface-confined hyperbolic polaritons [23, 24], and even ghost hyperbolic phonon polaritons [25]. Besides, the van der Waals polaritons are manipulated by artificially engineering the interface, such as polariton lenses [26], prisms [27, 28], meta-optics [29–31], and moiré engineering [32–34]. However, near-field mapping on TMD flakes is still quite difficult to carry out in the visible region. Since TMD flakes show strong absorption in the visible region and the inherent difficulties in measuring such high refractive index materials, it leads to a small transmission distance and a low contrast of the measured near-field fringes. Due to some important optical properties of the TMD flakes in the visible region, such as exciton-polariton transport and Zenneck surface waves [35–38], it is still highly required to develop a method on the near-field characterization on TMD flakes with an enhanced contrast of near-field fringes.

In this work, we report the systematical near-field optical characterization of the tungsten disulfide (WS_2) by using *s*-SNOM under the excitation of a continuous laser at 671 nm. The polarization-dependent near-field fringes are observed under *s*- and *p*-polarized excitation, indicating the TE and TM modes in the WS_2 flakes with varied thicknesses. Dielectric waveguide theory is employed to calculate and extract the dispersion relations of various modes. It reveals a high refractive index of 4.96/3.01 (in- and out-of-plane), indicating a giant birefringence ($\Delta n = 1.95$) of WS_2 flakes at 671 nm. Interestingly, the contrast of the observed near-field fringes in the WS_2 waveguide is enhanced with Au substrate in comparison to SiO_2 substrate, which is ascribed to the localized and enhanced electromagnetic (EM) near field between the metallic tip and the Au substrate (gap-mode enhancement), enabling tip-enhanced light scattering [39–42]. Therefore, our work not only provides a feasible solution for

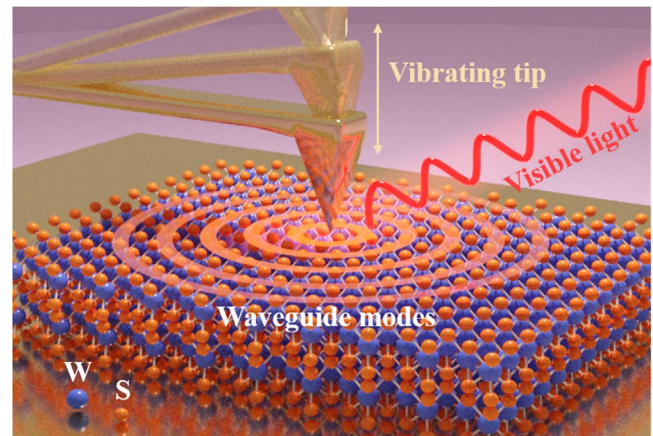


Figure 1. A schematic showing the near-field experimental set-up. A vibrating tip is illuminated by a beam of visible light and then excites the WS_2 waveguide modes.

the diagnosis of waveguide modes in high absorption bands of 2D materials but also offers experimental evidence on the potential application of WS_2 flakes in optical manipulation and energy-efficient modulators in photonic chips.

2. Experimental section

2.1. Sample preparation

Our WS_2 flakes were exfoliated from a bulk WS_2 crystal using Polydimethylsiloxane and transferred onto a gold-coated substrate (silicon +300 nm wet thermal oxide +50 nm e-beam evaporated gold with 5 nm chromium for adhesion) or standard Si wafers with a 300 nm thick SiO_2 layer. The samples were then heated at 50 °C for three minutes to eliminate the remaining organic residuals.

2.2. *s*-SNOM characterization

A VistaScope from Molecular Vista is used for the *s*-SNOM measurements. The *s*-SNOM is based on a tapping-mode atomic force microscope (AFM) illuminated by a monochromatic laser of wavelength 671 nm, as shown in figure 1. The AFM topographies of all flakes can be generated simultaneously with the *s*-SNOM images. The tip-tapping frequency is around 270 kHz and the tip-tapping amplitude is 50 nm for all experiments. The radius of curvature of the Au-coated silicon tip is about 10 nm. By demodulating the near-field signal at the third harmonic of the tip-tapping frequency of the AFM tip, the background signal can be greatly suppressed. Our *s*-SNOM experiments were all performed at ambient conditions.

3. Results and discussion

To introduce experimental parameters more conveniently, we simplified the experimental device diagram as shown in figures 2(a) and (b), which illustrate the 3D view and the front

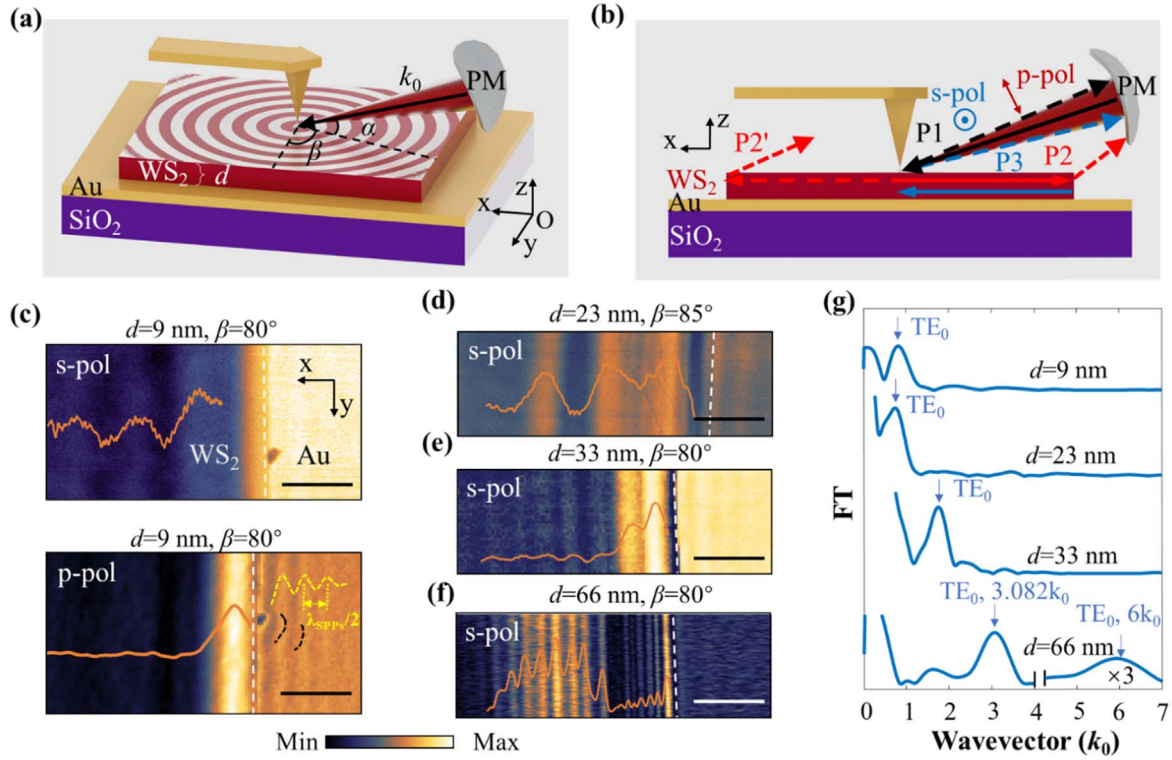


Figure 2. Experimental schematic diagram and nanoimaging of WS₂ planar waveguide on Au substrate. (a) 3D schematic diagram. The x -direction represents the direction of signal propagation, the y -direction represents the sample edge, and the z -axis is perpendicular to the sample surface. (b) Front view of the 3D experimental installation. Three main paths for what are labeled as P1 (black), P2 (red), P2' (red), and P3 (blue) arrows. (c)–(f) Near-field images of WS₂ flakes with different thicknesses. The real-space fringe profiles on the sample are marked by a solid orange line. The white dashed lines mark the sample edge. The yellow and black dashed lines mark the SPPs propagation. Scale bars, 1 μm . (g) The momentum space profiles are obtained by FT of the (c)–(f) fringe profiles in WS₂ samples. These peaks refer directly to the experimental momentum of the TE₀ mode and are indicated by blue arrows.

view of the near-field experimental set-up, respectively. The incident laser at $\lambda_0 = 671 \text{ nm}$ is focused on the apex of a gold-coated silicon tip by the parabolic mirror (PM), and the focus spot size under the tip is about $2 \mu\text{m} \times 1 \mu\text{m}$. Meanwhile, the scattered photons from the tip-sample system are also collected by the PM, and then coupled to a silicon detector. The polarization of the incident laser can be adjusted by rotating a half-wave plate to s -polarization (namely, electric-field perpendicular to the x - z plane) or p -polarization (namely, electric-field parallel to x - z plane). Also, the metalized tip illuminated by the incident light can provide sufficient momentum to satisfy the momentum matching condition. Therefore, the waveguide modes in WS₂ flakes can be excited as cylindrical waves near the sample surface, which is represented by the fringes as shown in figure 2(a). The angle between the incident light wavevector and the x - y plane is kept as $\alpha = 38^\circ$. β is defined as the angle between the sample edge and the projection of the incident light on the x - y plane, which can be adjusted by manually rotating the sample. Note that the scanning area is kept much smaller than the entire area of WS₂ flakes in our experiment, avoiding the signal interference from other boundaries. In figure 2(b), it illustrates three possible paths of photons collected by the detector. Specifically, path P1 indicates that the incident photons are scattered by a tip and then propagate back to the PM directly. When the guide mode in WS₂ flakes is excited, it

propagates radially away from the tip, and then a part of it is converted into photons at the right edge (path P2) and the left edge (path P2') of the sample, and the other part is reflected by the sample edge and reaches the tip again (path P3). The observed fringes on the sample surface are attributed to the interference of the photon collected by these paths.

Figures 2(c)–(f) present the measured s -SNOM images of WS₂ flakes with different thicknesses (see figure S1 for the optical images and AFM topographies). The top and the bottom panel of figure 2(c) show two near-field images of the same WS₂ flake (9 nm thickness) under the s -polarized to p -polarized excitation, respectively. Interestingly, the waveguide mode of the 9 nm WS₂ flake is excited under s -polarized excitation. As the polarization of incident light is changed to p -polarization, waveguide mode fringes are disappeared and surface plasmon polaritons (SPPs) fringes on Au substrate are appeared. Since y -directional dipole is induced in the tip under s -polarized excitation, only TE modes can be excited, which contain electric fields along the in-plane direction (E_y) [43]. While z -directional dipole is induced under p -polarized excitation, both TM modes (contain electric fields E_x and E_z) in the WS₂ flakes and the SPPs modes (contain electric fields E_x and E_z) on Au substrate can be excited. Thereby, both of the waveguide modes (TE and TM mode) in WS₂ flakes and the SPPs mode on Au substrate can be simultaneously excited by adjusting the polarization of

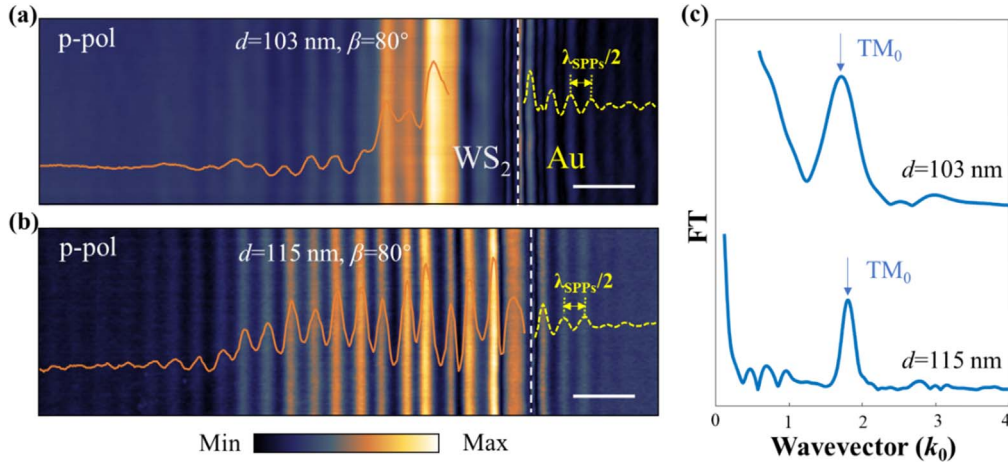


Figure 3. Near-field imaging of the WS₂ planar waveguide on Au substrate under the *p*-polarization laser. (a) 103 nm (b) 115 nm. The fringe profiles on the sample are marked with solid orange lines. The fringe profiles of SPPs propagation on Au substrate are indicated by yellow dashed lines. The white dashed lines mark the sample edge. Scale bars, 1 μm . (c) FT analysis of the real-space profiles in (a) and (b), respectively. The arrows indicate the FT peaks of the WS₂ waveguide mode.

incident light, propagating with different wavelengths and opposite wavevectors (figure S2 (available online at stacks.iop.org/NANO/33/345201/mmedia)). SPPs are electromagnetic waves that arise via the collective oscillation of electrons on the surface of the conductor by electromagnetic field. The theoretical value of SPPs wavelength can be calculated by $\lambda_{\text{SPPs}} \approx \lambda_0 \sqrt{(\text{Re}(\epsilon_m) + 1) / \text{Re}(\epsilon_m)}$ = 647 nm [44], where the wavelength of the incident light is $\lambda_0 = 671$ nm and the Au dielectric constant is $\epsilon_m = -15.88 + 1.29i$ [45]. And the period of the SPP fringes in the bottom panel of figure 2(c) is measured to be 320 nm, which is equal to the half of the wavelength of SPPs and in good agreement with the theoretically expected value (figure S4(d) illustrates the mechanism by which SPPs fringes occur on Au substrate). Note that the impurity on Au substrate can also excite SPPs, indicated by the black stripes in the bottom panel of figure 2(c). Hence, Au substrate is very helpful to distinguish the specific polarization of the incident laser.

In figures 2(c)–(f), the propagation of TE₀ mode in the WS₂ flakes with different thicknesses ($d = 9$ nm, 23 nm, 33 nm, and 66 nm) under *s*-polarized excitation is observed. Within these images, we see clearly the interference fringes in parallel to WS₂ flake edges (white dashed lines), and the fringes period shows an apparent thickness dependence. Specifically, the fringe period is decreased from 891.1 to 217.7 nm as the thickness of the flakes is increased, while the number of fringes shows a significant increase for thicker WS₂ flakes. To extract the fringe period, figure 2(g) shows the relevant results by Fourier transform (FT) from the intensity profile of the fringes in figures 2(c)–(f), and the peak positions of $0.805k_0$, $0.753k_0$, $1.747k_0$, and $3.082k_0$ indicate the obtained wavevectors of the fringes, where k_0 is the wavevector of incident light. It should be noted that the fringes period near the edge of the sample ($d = 66$ nm) is half of that in the middle part of the same sample, as shown in figure 2(f). It can further be supported by the related FT result that an additional peak at $6k_0$ can be found, which is twice $3.082k_0$. According to the calculation of optical path difference (OPD), the fringes period generated by the interference between the

path P1 and P2 is in accordance with the guided wavelength, while the fringes period by the path P1 and P3 is about half of the guided wavelength (SI, section 2). Therefore, the observed fringes with a smaller period near the sample edge are ascribed to the weak back reflection by the sample edge. In general, the interference between P1 and P3 is quite hard to be observed in the visible region because the wavevectors of guided modes in WS₂ flakes are too small for sufficient reflection by sample edge. The previous works just reported the interference of surface phonon polaritons in hBN or SPPs on graphene between the path P1 and P3 at the infrared region, the wavevectors of which are much larger than the wavevector of incident light [21, 22, 46].

Figures 3(a) and (b) present the measured *s*-SNOM images in the WS₂ flakes with the thickness of 103 nm and 115 nm under *p*-polarized excitation, respectively. Within these two images, we see the near-field fringes of TM₀ modes in WS₂ and that of SPPs in Au substrate. Following the above methodology, the wavevectors of fringes in WS₂ are extracted to be $1.714k_0$ and $1.805k_0$ by performing FT analysis as shown in figure 3(c). Furthermore, the fringes period on Au substrate is also measured to be 320 nm, which is consistent with the previous theoretical prediction. It should be noted that the fringes near the edge appear to be irregular in figure 3(a), which is ascribed to the irregular edge reflection (see the corresponding AFM topography and height profile in figure S1(e)). Therefore, the accurate fringes period can be obtained by subtracting the first stripe near the sample edge in performing Fourier transform.

For comparison, a similar experiment is also carried out in the WS₂ flakes on a standard SiO₂/Si wafer. Figures 4(a), (b), and (d) present the measured results in the WS₂ flakes ($d = 53$ nm, 98 nm, and 62 nm) under *p*-polarized excitation. As shown in figure 4(c), the wavevectors of fringes in figures 4(a) and (b) are extracted to be $2.071k_0$ and $2.833k_0$ by performing FT. Besides, there is also another FT Peak (about $1.6k_0$) that does not vary with sample thickness, which is typical of the air mode. From the left fringes of samples in figures 4(a), (b), and (d), one can still find that the fringe period is decreased with the increase

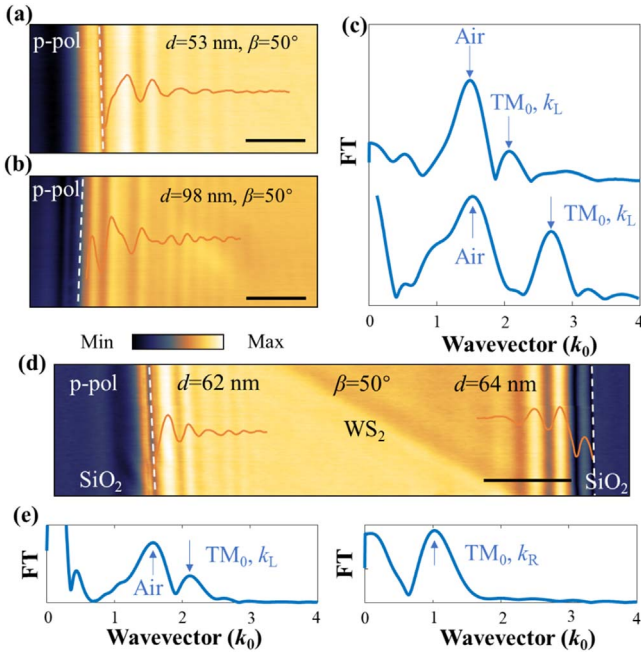


Figure 4. Near-field imaging of the WS₂ planar waveguide on a standard SiO₂/Si wafer substrate under the *p*-polarization laser. (a), (b) Near-field imaging of WS₂ flakes at $d = 53$ nm and 98 nm and their fringe profiles. Scale bars are 1 μ m. (c) FT analysis of the fringe profiles in (a) and (b). (d) Near-field image of 62 nm WS₂ nanobelt. The scale bar is 2 μ m. (e) FT analysis result of the fringes profiles of the left and the right edge of (d), respectively.

of sample thickness. By studying a WS₂ nanobelt in figure 4(d), the influence of left and right edges on the near-field fringes can be observed more intuitively. In detail, the difference between the fringe spacing near the right and left edge of the WS₂ nanobelt is derived from the different OPD of P1-P2 and P1-P2'. Through the calculation of OPD (SI, section 2), the WS₂ waveguide mode effective indices of refraction, n_{eff} , can be written as,

$$n_{\text{eff}} = \frac{k_{\text{R,L}}}{k_0} \pm \cos \alpha \sin \beta, \quad (1)$$

where $k_{\text{(R,L)}} = 2\pi/\rho_{\text{(R,L)}}$ is the wavevector of the fringes near the right and left edge and $\rho_{\text{(R,L)}}$ is the fringe period measured from the right and left edge, respectively. In other words, it can be seen from equation (1) that if we measure the left and right edges of a sample at the same time, the wavevector of the right edge will be $2 \cos \alpha \sin \beta$ less than that of the left edge, that is, the measured fringe period of the right edge will be $\pi/\cos \alpha \sin \beta$ larger than that of the left edge. In figure 4(e), the dominant FT peak is located at $1.02k_0$ and $2.12k_0$ for k_{R} and k_{L} respectively. By using equation (1), n_{eff} of the right and left fringes are determined to be 1.51 and 1.62, respectively. Noting that there is a slight deviation between the n_{eff} value of the right and left fringes. This is mainly caused by the 2 nm difference in thickness between this sample's right and left sides, which is supported by AFM measurement (figure S3). Another reason is the partial overlap between the TM₀ mode and the air mode can be observed in the left-fringes-profiles FT, leading to a closer position of the peak of the TM₀ mode and the air mode, which is similar to the previous study [17].

To understand the experimental results more intuitively, WS₂ flakes with three typical thicknesses (115 nm, 64 nm, 9 nm) are selected for theoretical analysis. Figure 5(a) shows the simulated result of three modes of TE₀, TE₁, and TM₀ that can propagate inside the 115 nm thick WS₂ waveguide, indicating the guided modes are confined well in WS₂. Compared with the related experimental result in figure 3(b), it is found that TM₀ mode can be selectively excited by using the *p*-polarized incident laser. Figures 5(b) and (c) present the calculated results in the WS₂ flakes at $d = 64$ nm and 9 nm, showing the waveguide mode of TM₀ and TE₀, respectively. Considering a finite thickness of the SiO₂ layer (300 nm), one can observe that the waveguide modes are passed through the SiO₂ layer and dissipated in the Si layer below, forming the leaky modes. In general, when the effective refractive index of the waveguide mode is less than the refractive index of the silicon, the energy inside the WS₂ flake tends to leak into the Si layer. Therefore, it indicates that the waveguide modes in the thicker samples can propagate farther.

Figure 6(a) lists the obtained values of the fringes contrast from our experimental results on Au substrate and SiO₂ substrate (see calculated process in SI, section 3), and it is defined as

$$\text{Contrast} = \frac{\overline{E_{\text{peak}}} - \overline{E_{\text{valley}}}}{\overline{E_{\text{peak}}} + \overline{E_{\text{valley}}}}, \quad (2)$$

where $\overline{E_{\text{peak}}}$ is the averaged peak values of the bright fringes and $\overline{E_{\text{valley}}}$ is the averaged valley values of the dark fringes. The fringes contrast on the Au substrate is much higher than that on the SiO₂/Si substrate. The main mechanism for the tip-enhanced EM is near-field coupling between the Au-coated tip and the Au substrate. Thus, it is useful to perform *s*-SNOM characterization on the Au-film substrates, showing an enhanced contrast of the fringes.

In figure 6(b), equation (1) is used to summarize the experimentally obtained data on the effective indices of refraction, n_{eff} . Specifically, the data points of TE₀ and TM₀ mode on Au substrate are marked with stars and squares, while the data points of TM₀ on the SiO₂ substrate are marked with triangles. For the optical anisotropy in the WS₂ flakes in the visible region, the experimental results are further analyzed by using the planar waveguide model, extracting the values of the anisotropic dielectric constant of the WS₂ flakes. The theoretical model we use here is a sandwich structure (see the illustration in figure S6), with air on the top, WS₂ in the middle, and a substrate on the bottom. Different from the traditional waveguide structure, the core layer used in this theoretical model is an anisotropic medium. This is analogous to ordinary and extraordinary rays in bulk anisotropic crystals, it has been proven in reference [17]. The thickness dispersion of TE and TM modes in this system can be obtained by the following equations

$$k_0 d \sqrt{\varepsilon_{\perp} - n_{\text{eff,TE}}^2} = \tan^{-1} \left(\frac{\sqrt{n_{\text{eff,TE}}^2 - \varepsilon_1}}{\sqrt{\varepsilon_{\perp} - n_{\text{eff,TE}}^2}} \right) + \tan^{-1} \left(\frac{\sqrt{n_{\text{eff,TE}}^2 - \varepsilon_2}}{\sqrt{\varepsilon_{\perp} + n_{\text{eff,TE}}^2}} \right) + m\pi \quad (3)$$

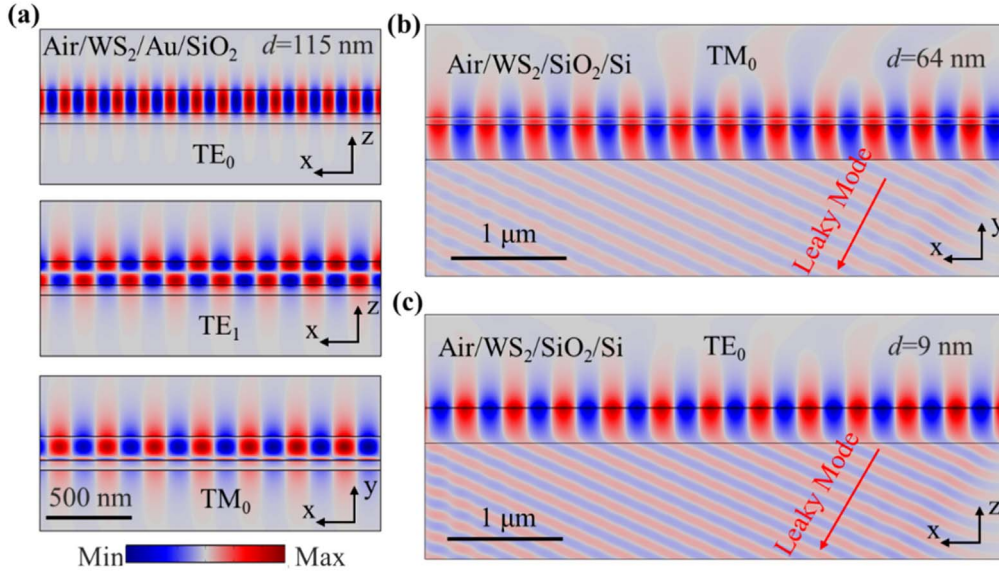


Figure 5. Numerical simulations of guided modes propagation in WS₂. (a) Numerical simulations of different modes propagation in 115 nm thick WS₂. The wavelength of incident light input at the left port is 671 nm. (b), (c) Numerical simulations of WS₂ with $d = 9$ nm for TE₀ and $d = 64$ nm for TM₀ under 300 nm SiO₂ substrate. The red arrows indicate the propagation directions of the leaky mode in the Si layer. To see the evanescent wave distribution more clearly, 200% color saturation was selected in (a), (b), and (c).

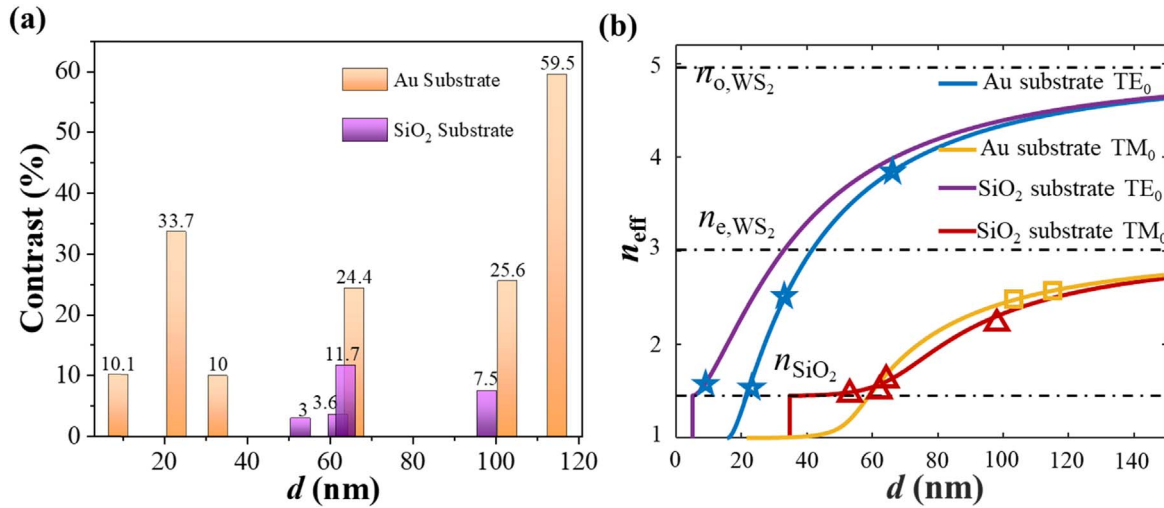


Figure 6. Analyses of experimental results. (a) Comparison of the contrast of the fringes in the near-field images on Au and SiO₂ substrates. (b) Experimental data and theoretical dispersion relations of TE₀ and TM₀ waveguide modes, respectively, for WS₂ flakes on Au and SiO₂ substrate.

and

$$k_0 d \sqrt{\frac{\varepsilon_{\perp}}{\varepsilon_{\parallel}}} \sqrt{\varepsilon_{\parallel} - n_{\text{eff, TM}}^2} = \tan^{-1} \left(\frac{\sqrt{\varepsilon_{\perp} \varepsilon_{\parallel}} \sqrt{n_{\text{eff, TM}}^2 - \varepsilon_1}}{\varepsilon_1 \sqrt{\varepsilon_{\parallel} - n_{\text{eff, TM}}^2}} \right) + \tan^{-1} \left(\frac{\sqrt{\varepsilon_{\perp} \varepsilon_{\parallel}} \sqrt{n_{\text{eff, TM}}^2 - \varepsilon_2}}{\varepsilon_2 \sqrt{\varepsilon_{\parallel} - n_{\text{eff, TM}}^2}} \right) + n\pi, \quad (4)$$

where $k_0 = 2\pi/\lambda_0$ ($\lambda_0 = 671$ nm) is the incident light wavevector; d is the WS₂ thickness; ε_{\perp} is the in-plane relative dielectric constant (perpendicular to the optic axis of WS₂, namely z -axis), and ε_{\parallel} is out-of-plane relative dielectric constant (parallel to z -axis), respectively; $n_{\text{eff, TE}}$ and $n_{\text{eff, TM}}$ are effective

indices of refraction for TE and TM modes, respectively; $\varepsilon_1 = 1$ and ε_2 ($\varepsilon_{\text{Au}} = -15.88$, $\varepsilon_{\text{SiO}_2} = 2.12$ at 671 nm) [45, 47] are the relative dielectric constants of superstrate and substrate, respectively; m and n are the order numbers of TE and TM modes, respectively ($m, n = 0, 1, 2, \dots$). By substituting the n_{eff} of TE₀ mode with $d = 66$ nm and TM₀ mode with $d = 115$ nm into equations (3) and (4), respectively, it is obtained that the dielectric constants of the WS₂ flakes are $\varepsilon_{\parallel} = 24.65$, $\varepsilon_{\perp} = 9.09$. Therefore, the in-plane refractive index and the out-of-plane refractive index of WS₂ are $n_o = \sqrt{\varepsilon_{\parallel}} = 4.96$, $n_e = \sqrt{\varepsilon_{\perp}} = 3.01$, respectively. And the birefringence value of WS₂ ($\Delta n = n_o - n_e$) reaches 1.95. Compared to the other materials (Δn of calcite is 0.17, designed liquid crystal is 0.7, and the

maximum value of GaP nanowire Δn is 0.8) [7–10] and some results of measurements of the same type of work (Δn of hBN at 633 nm is 0.58, Δn of MoS₂ at 1530 nm is 1.4, and Δn of PtSe₂ at mid-infrared is 0.56) [17, 48], the giant optical birefringence indicates that WS₂ is a promising candidate for integrated phase retardation application.

Figure 6(b) shows the calculated thickness-dependent dispersion curves of the WS₂ flakes on Au or SiO₂ substrates by solving equations (3) and (4) numerically, showing a good agreement with the experimental data. While there are some higher-order waveguide modes in the thicker samples, we only present the modes of TE₀ and TM₀ (see dispersion curves of more waveguide modes in SI, section 4). In figure 6(b), the significant anisotropy of WS₂ is showed that the effective refractive index of TE mode and TM modes approaches asymptotically to n_o and n_e with the increase of thickness, respectively. As previously analyzed, due to the interference of air mode, the values of n_{eff} for the left edge fringes ($d = 53, 98, 62$ nm) measured in figures 4(a), (b), and (d) are slightly smaller than the theoretically calculated curves. Note that the cutoff thickness for TE₀ dispersion curves on Au and SiO₂ substrates is 15.4 nm and 5 nm, respectively. And the waveguide mode of the WS₂ flake at $d = 9$ nm on Au substrate is consistent with the theoretical curve of the SiO₂ substrate in figure 6(b), probably because the thickness of Au substrate used is too thin to shield ultrathin WS₂ flakes from the effect of SiO₂.

4. Conclusions

In summary, we present a systematical near-field characterization on the WS₂ flakes with different thicknesses by using the *s*-SNOM technique. With the assistance of an Au substrate, the contrast of the near-field fringes is enhanced in comparison with that in conventional SiO₂/Si wafer. It is observed that TE₀ and TM₀ waveguide modes in the WS₂ flakes can be separately excited by choosing a specific thickness under specific polarized incident light. And then, the in-plane and out-of-plane refractive indexes of WS₂ are determined to be 4.96 and 3.01, respectively, indicating a high birefringence value up to 1.95. It is well supported by the theoretical simulations. Therefore, our work paves the way for the potential applications of WS₂ flakes in optical circuit integrations in the visible region, such as the tunable single-mode waveguides, the nano-integrated polarization-sensitive devices, and exciton dynamics.

Acknowledgments

This work was supported by the National Natural Science Foundation of China (Nos. 91850113, 11774115, and 11904271), the 973 Programs under grants 2014CB921301, the Basic and Applied Basic Research Major Program of Guangdong Province (No.2019B030302003). Special thanks to the Analytical and Testing Center of HUST and the Center

of Micro-Fabrication and Characterization (CMFC) of WNLO for using their facilities.

Data availability statement

All data that support the findings of this study are included within the article (and any supplementary files).

Competing financial interests

The authors declare that they have no conflict of interest or financial conflicts to disclose.

ORCID IDs

Hua Long  <https://orcid.org/0000-0002-7959-7828>

Kai Wang  <https://orcid.org/0000-0003-2122-1294>

References

- [1] Nicholls L H, Rodríguez-Fortuño F J, Nasir M E, Córdova-Castro R M, Olivier N, Wurtz G A and Zayats A V 2017 Ultrafast synthesis and switching of light polarization in nonlinear anisotropic metamaterials *Nat. Photonics* **11** 628–33
- [2] Wu S, Efron U and Hess L D 1984 Infrared birefringence of liquid crystals *Appl. Phys. Lett.* **44** 1033–35
- [3] Niu S *et al* 2018 Giant optical anisotropy in a quasi-one-dimensional crystal *Nat. Photonics* **12** 392–96
- [4] Hu D, Chen K, Chen X, Guo X, Liu M and Dai Q 2019 Tunable modal birefringence in a low-loss van der waals waveguide *Adv. Mater.* **31** 1807788
- [5] Wang C, Zhang M, Chen X, Bertrand M, Shams-Ansari A, Chandrasekhar S, Winzer P and Lončar M 2018 Integrated lithium niobate electro-optic modulators operating at CMOS-compatible voltages *Nature* **562** 101–04
- [6] Zhang Y, He Y, Zhu Q, Jiang X, Guo X, Qiu C and Su Y 2018 On-chip silicon polarization and mode handling devices *Front. Optoelectron.* **11** 77–91
- [7] Ghosh G 1999 Dispersion-equation coefficients for the refractive index and birefringence of calcite and quartz crystals *Opt. Commun.* **163** 95–102
- [8] Sekine C, Iwakura K, Konya N, Minai M and Fujisawa K 2001 Synthesis and properties of some novel high birefringence phenylacetylene liquid crystal materials with lateral substituents *Liq. Cryst.* **28** 1375–87
- [9] Herman J and Kula P 2017 Design of new super-high birefringent isothiocyanato bistolanes—synthesis and properties *Liq. Cryst.* **44** 1462–67
- [10] Muskens O L, Borgström M T, Bakkers E P A M and Gómez Rivas J 2006 Giant optical birefringence in ensembles of semiconductor nanowires *Appl. Phys. Lett.* **89** 233117
- [11] Wang Q H, Kalantar-Zadeh K, Kis A, Coleman J N and Strano M S 2012 Electronics and optoelectronics of two-dimensional transition metal dichalcogenides *Nat. Nanotech.* **7** 699–712
- [12] Ling H, Li R and Davoyan A R 2021 All van der Waals integrated nanophotonics with bulk transition metal dichalcogenides *ACS Photonics* **8** 721–30

- [13] Novoselov K S, Jiang D, Schedin F, Booth T J, Khotkevich V V, Morozov S V and Geim A K 2005 Two-dimensional atomic crystals *Proc. Natl. Acad. Sci. USA* **102** 10451–3
- [14] Velický M, Bissett M A, Woods C R, Toth P S, Georgiou T, Kinloch I A, Novoselov K S and Dryfe R A W 2016 Photoelectrochemistry of pristine mono- and few-layer MoS₂ *Nano Lett.* **16** 2023–32
- [15] Budania P, Baine P T, Montgomery J H, McNeill D W, Neil Mitchell S J, Modreanu M and Hurley P K 2017 Comparison between Scotch tape and gel-assisted mechanical exfoliation techniques for preparation of 2D transition metal dichalcogenide flakes *Micro Nano Lett.* **12** 970–73
- [16] Weber J W, Calado V E and van de Sanden M C M 2010 Optical constants of graphene measured by spectroscopic ellipsometry *Appl. Phys. Lett.* **97** 091904
- [17] Hu D et al 2017 Probing optical anisotropy of nanometer-thin van der Waals microcrystals by near-field imaging *Nat. Commun.* **8** 1471
- [18] Ermolaev G A et al 2021 Giant optical anisotropy in transition metal dichalcogenides for next-generation photonics *Nat. Commun.* **12** 854
- [19] Dai S et al 2014 Tunable phonon polaritons in atomically thin van der waals crystals of boron nitride *Science* **343** 1125–9
- [20] Caldwell J D et al 2014 Sub-diffractive volume-confined polaritons in the natural hyperbolic material hexagonal boron nitride *Nat. Commun.* **5** 5221
- [21] Dai S et al 2017 Efficiency of launching highly confined polaritons by infrared light incident on a hyperbolic material *Nano Lett.* **17** 5285–90
- [22] Ambrosio A, Tamagnone M, Chaudhary K, Jauregui L A, Kim P, Wilson W L and Capasso F 2018 Selective excitation and imaging of ultraslow phonon polaritons in thin hexagonal boron nitride crystals *Light: Sci. Appl.* **7** 27
- [23] Li P, Dolado I, Alfaro-Mozaz F J, Nikitin A Y, Casanova F, Hueso L E, Vélez S and Hillenbrand R 2017 Optical nanoimaging of hyperbolic surface polaritons at the edges of van der Waals materials *Nano Lett.* **17** 228–35
- [24] Dai S et al 2018 Manipulation and steering of hyperbolic surface polaritons in hexagonal boron nitride *Adv. Mater.* **30** 1706358
- [25] Ma W et al 2021 Ghost hyperbolic surface polaritons in bulk anisotropic crystals *Nature* **596** 33662–66
- [26] Folland T G, Fali A, White S T, Matson J R, Liu S, Aghamari N A, Edgar J H, Haglund R F Jr, Abate Y and Caldwell J D 2018 Reconfigurable infrared hyperbolic metasurfaces using phase change materials *Nat. Commun.* **9** 4371
- [27] Alonso-González P et al 2014 Controlling graphene plasmons with resonant metal antennas and spatial conductivity patterns *Science* **344** 1369–73
- [28] Duan J et al 2021 Planar refraction and lensing of highly confined polaritons in anisotropic media *Nat. Commun.* **12** 4325
- [29] Li P, Dolado I, Alfaro-Mozaz F J, Casanova F, Hueso L E, Liu S, Edgar J H, Nikitin A Y, Vélez S and Hillenbrand R 2018 Infrared hyperbolic metasurface based on nanostructured van der Waals materials *Science* **359** 892–96
- [30] Chaudhary K et al 2019 Polariton nanophotonics using phase-change materials *Nat. Commun.* **10** 4487
- [31] Xiong L et al 2019 Photonic crystal for graphene plasmons *Nat. Commun.* **10** 4780
- [32] Sunku S S et al 2018 Photonic crystals for nano-light in moiré graphene superlattices *Science* **362** 1153–56
- [33] Hu G et al 2020 Topological polaritons and photonic magic angles in twisted α -MoO₃ bilayers *Nature* **582** 209–13
- [34] Duan J, Capote-Robayna N, Taboada-Gutiérrez J, Álvarez-Pérez G, Prieto I, Martín-Sánchez J, Nikitin A Y and Alonso-González P 2020 Twisted nano-optics: manipulating light at the nanoscale with twisted phonon polaritonic slabs *Nano Lett.* **20** 5323–29
- [35] Hu F, Luan Y, Scott M E, Yan J, Mandrus D G, Xu X and Fei Z 2017 Imaging exciton–polariton transport in MoSe₂ waveguides *Nat. Photonics* **11** 356–60
- [36] Mrejen M, Yadgarov L, Levanon A and Suchowski H 2019 Transient exciton-polariton dynamics in WSe₂ by ultrafast near-field imaging *Sci. Adv.* **5** eaat9618
- [37] Sternbach A J et al 2020 Femtosecond exciton dynamics in WSe₂ optical waveguides *Nat. Commun.* **11** 3567
- [38] Babicheva V E, Gamage S, Zhen L, Cronin S B, Yakovlev V S and Abate Y 2018 Near-field surface waves in few-layer MoS₂ *ACS Photonics* **5** 2106–12
- [39] Zhang W, Cui, Yeo B-S, Schmid T, Hafner C and Zenobi R 2007 Nanoscale roughness on metal surfaces can increase tip-enhanced Raman scattering by an order of magnitude *Nano Lett.* **7** 1401–5
- [40] Yang Z, Aizpurua J and Xu H 2009 Electromagnetic field enhancement in TERS configurations *J. Raman Spectrosc.* **40** 1343–48
- [41] Alajlan A M, Voronine D V, Sinyukov A M, Zhang Z, Sokolov A V and Scully M O 2016 Gap-mode enhancement on MoS₂ probed by functionalized tip-enhanced Raman spectroscopy *Appl. Phys. Lett.* **109** 133106
- [42] Kusch P, Morquillas Azpiazu N, Mueller N S, Mastel S, Pascual J I and Hillenbrand R 2018 Combined tip-enhanced Raman spectroscopy and scattering-type scanning near-field optical microscopy *J. Phys. Chem. C* **122** 16274–80
- [43] Hu F, Luan Y, Speltz J, Zhong D, Liu C H, Yan J, Mandrus D G, Xu X and Fei Z 2019 Imaging propagative exciton polaritons in atomically thin WSe₂ waveguides *Phys. Rev. B* **100** 121301
- [44] Yin L, Vlasko-Vlasov V K, Rydh A, Pearson J and Welp U 2004 Surface plasmons at single nanoholes in Au films *Appl. Phys. Lett.* **85** 467
- [45] Yakubovsky D I, Arsenin A V, Stebunov Y V, Fedyanin D Y and Volkov V S 2017 Optical constants and structural properties of thin gold films *Opt. Express* **25** 25574–87
- [46] Hu F, Kim M, Zhang Y, Luan Y, Ho K M, Shi Y, Wang C Z, Wang X and Fei Z 2019 Tailored plasmons in pentacene/graphene heterostructures with interlayer electron transfer *Nano Lett.* **19** 6058–64
- [47] Malitson I H 1965 Interspecimen comparison of the refractive index of fused silica *J. Opt. Soc. Am.* **55** 1205–9
- [48] Wong K P, Hu X, Lo T W, Guo X, Fung K H, Zhu Y and Lau S P 2021 Edge-orientation dependent nanoimaging of mid-infrared waveguide modes in high-index PtSe₂ *Adv. Opt. Mater.* **9** 2100294